Bulletin of the JSME Vol.00, No.00, 2017

*JSME Journal Template*

# Simultaneous two cross-sectional measurements of $NH_3$ concentration in bent pipe flow using CT-tunable diode laser absorption spectroscopy

Hitoshi MATSUI*, Kazumasa UDAGAWA*, Yoshihiro DEGUCHI** and Takahiro KAMIMOTO**

* CAE Digital Development Dept., ISUZU MOTORS LIMITED,
8 Tsuchidana, Fujisawa, 252-0881, Japan
E-mail: Hitoshi_Matsui@notes.isuzu.co.jp
** Graduate School of Technology, Industrial and Social Sciences, Tokushima University
2-1, Minamijyosanjima-cho, Tokushima, Tokyo 160-0016, Japan

**Received: X January 2019; Revised: X February 2019; Accepted: X March 2019**

**Abstract**

Urea Selective Catalytic Reduction (urea SCR) system is widely used for diesel engine to reduce the emission of $NO_x$ by $NH_3$ which is provided by a hydrolysis of urea water. Concentration distribution of $NH_3$ in an exhaust pipe is an important factor for improvement of the SCR efficiency and prevention of $NH_3$ slip and urea deposit. Therefore, it is necessary to measure two-dimensional (2D) concentration of $NH_3$ in detail. The purpose of this study is to develop the real-time two cross-sectional measurements technology of $NH_3$ concentration using the computed tomography-tunable diode laser absorption spectroscopy (CT-TDLAS). Theoretical $NH_3$ concentration distribution which was reconstructed by CT agreed to CFD results and quadruple pipe's results showed good resolution by 14th order reconstruction. Therefore, this method has enough resolution and accuracy for measuring the concentration distribution of $NH_3$. And this method was employed in a bent pipe model demonstrated a urea SCR system. The experimental results of two cross-sectional 2D concentration of $NH_3$ show differences of the concentration distribution of $NH_3$ each cross-section and flow pattern like swirl flow. It was found that CT-TDLAS was an effective method to measure concentration distribution of $NH_3$ and observe characteristics of flow. In addition, observing flow pattern enable to validate CFD results, and it helps to improve efficiency of after treatment system.

***Keywords*** : Measurement and instrumentation, CT tunable diode laser absorption spectroscopy, $NH_3$ concentration measurement, Urea selective catalytic reduction, Exhaust aftertreatment

## Nomenclature of CFD governing equation

| | | | |
|---|---|---|---|
| $x_i$ | : | Coordinates | [m] |
| $u_i$ | : | Velocity of flow in $x_i$ - direction | [m/s] |
| $t$ | : | Time | [s] |
| $\rho$ | : | Density of a fluid or a solid | [kg/m$^3$] |
| $\mu$ | : | Viscosity | [Pa·s] |
| $\sigma_{ij}$ | : | Stress tensor | |
| $g_i$ | : | Gravity | [m/s$^2$] |
| $k$ | : | Turbulent energy | [m$^2$/s$^2$] |
| $\varepsilon$ | : | Turbulent dissipation rate | [m$^2$/s$^3$] |
| C | : | Concentration of diffusive species | [-] |
| $D_m$ | : | Diffusion coefficient | [m$^2$/s] |
| $\dot{d}$ | : | Source term of diffusive species | [1/s] |

Paper No.xx-xxxx
[DOI: 10.1299/xxx.2017xxx000x]

## 1. Introduction

Recently, there is a global trend to strengthening of diesel engine emission regulations on $NO_x$ and PM emissions. With enforcing the regulations, several technologies have been developed in the latest few decades for reducing these emissions. In these technologies, urea Selective Catalytic Reduction (urea SCR) system is widely used for reducing $NO_x$ from diesel engines. Figure 1 shows a schematic of urea SCR system. The urea injector which is set upstream of the SCR catalyst injects urea water into an exhaust pipe. The urea water converts to $NH_3$ by pyrolysis and hydrolysis. Then $NH_3$ and $NO_x$ are converted into harmless nitrogen and water by the catalytic reaction. However, if urea water is injected too much to get high efficiency of the $NO_x$ reduction, there will be some problems which are increase of urea consumption, $NH_3$ slip and urea deposit. To prevent these problems, it is important to control the concentration distribution of $NH_3$ in front of the SCR catalyst. Therefore, it is necessary to visualize the $NH_3$ behavior in the exhaust pipe.

In recent years, the technology of laser diagnostics has progressed as a measurement technique with high sensitivity and response in practical reaction processes. One of such techniques is the high response measurement method by using a tunable diode laser absorption spectroscopy (TDLAS) (Deguchi, 2011; Deguchi et al., 2012). In addition, TDLAS has been used in several industrial applications (Rieker et al., 2007; Yamakage et al., 2008; Wright et al., 2010; Ma et al., 2013). These methods can measure the average value along the laser path. To measure the two-dimensional (2D) concentration of gases or temperature, TDLAS and Computed Tomography (CT) techniques were combined (Deguchi et al.; 2015; Kamimoto et al., 2015; Kamimoto et al.; 2016). However, these studies measured the single section of flow fields and the multi-sectional measurement is necessary to observe the characteristics of flow.

The purpose of this study is to develop the real-time two cross-sectional measurements technology of $NH_3$ concentration using the computed tomography-tunable diode laser absorption spectroscopy (CT-TDLAS). In this study, two cross-sectional 2D concentration of $NH_3$ has been measured by CT-TDLAS at the same time to observe flow characteristics. This measurement is first in the world and helps to develop the urea SCR system.

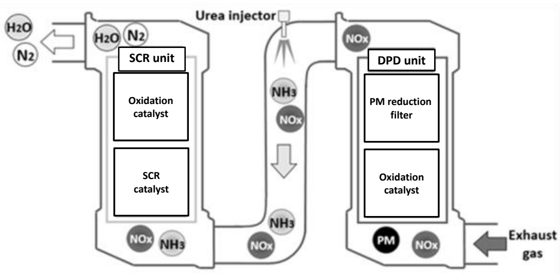


Fig. 1 Schematic of urea SCR system.

## 2. Theory

Tunable diode laser absorption spectroscopy (TDLAS) was used to measure the concentration of $NH_3$ in this study. TDLAS is a method for measuring the concentration of multi-species. When light passes through an absorption medium, the transmitted intensity is related to absorber concentration of species present by Lambert Beer's law.

$$I_\lambda / I_{\lambda 0} = exp\{-A_\lambda\} = exp\left\{-\sum_i \left(n_i L \sum_j S_{i,j}(T) G_{Vi,j}\right)\right\} \quad (1)$$

Here, $I_{\lambda 0}$ is the incident light intensity, $I_\lambda$ the transmitted light intensity, $A_\lambda$ the absorbance, $n_i$ the number density of species $i$, $L$ the path length, $S_{ij}$ the temperature dependent adsorption line strength of the absorption line $j$, and $G_{vi,j}$ the line broadening function.

In this study, $NH_3$ and $H_2O$ absorption spectra were used to measure concentration and temperature at the same time.

[DOI: 10.1299/xxx.2017xxx000x] 

Figure 2(a) shows $NH_3$ absorption spectra, and the absorption line of $NH_3$ located at 1512.22 nm was used to measure $NH_3$ concentration. Figure 2(b) shows the linear relation between the absorbance and the concentration. With CT algorism, this relation is used for measuring 2D concentration distribution. Figure 3 shows theoretical $H_2O$ absorption spectra by using the HITRAN database (Rothman et al., 2009) and three absorption lines located at 1388.135 nm (#1), 1388.326 nm (#2) and 1388.454 nm (#3) were used to measure temperature.

Absorption of transmitted light happens on the optical path. The absorption signal intensity becomes an integrated value of the optical path. In this study, several optical paths are intersected to each other to form the analysis grid, reconstructing 2D temperature distribution by a CT method (Ma et al., 2008; Wang et al., 2010; Kasyutich et al., 2011; An et al., 2011; Deguchi et al., 2012; Deguchi et al., 2015; An et al., 2015; Cai, et al., 2015; Jatana, et al., 2015; McCann, et al., 2015; Seidel, et al., 2015; Stritzke, et al., 2015; Kamimoto et al., 2016). Figure 4 shows concept of analysis grids and laser beam paths. The integrated absorbance in the path $p$ is given by

$$A_{\lambda,p} = \sum_q n_q L_{p,q} \alpha_{\lambda,q} \tag{2}$$

Because the integrated absorbance is dependent on both temperature and concentration, the temperature distribution has to be calculated by more than two different absorbance values. Temperature and $NH_3$ concentration at each analysis grid determined using a multi-function minimization method to minimize the spectral fitting error at 1512.0-1512.6 nm.

A set of measured absorption spectra was compared to the theoretical spectra to measure temperature and concentration. Sets of temperature, $NH_3$ and $H_2O$ concentration distributions at analysis grids were determined separately by each minimization procedure shown in Fig. 5(a). A polynomial noise reduction technique was also used to reduce noises such as the effect of laser beam steering.

Figure 5(b) shows the procedure of deciding initial values. Initial values were decided by minimizing the error between a set of measured absorption spectra and initial values combined several data from an initial value database. This algorism helps to remove dependency of initial values.

$$\text{Error} = \sum \left\{ \left(A_{\lambda,p}\right)_{theory} - \left(A_{\lambda,p}\right)_{experiment} \right\}^2 \tag{3}$$

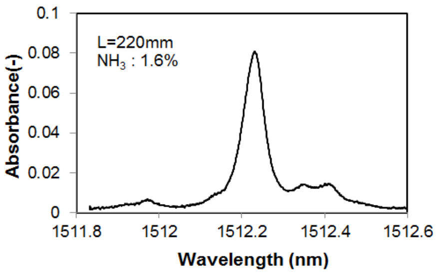


(a) $NH_3$ absorption spectrum

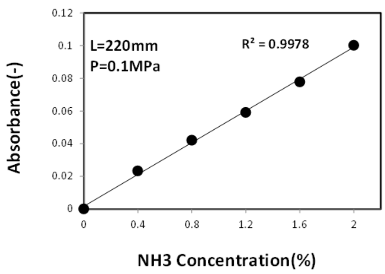


(b) Linearity $NH_3$ absorption spectra

Fig. 2 Proportionate relationship between the NH3 concentration and the absorption intensity.

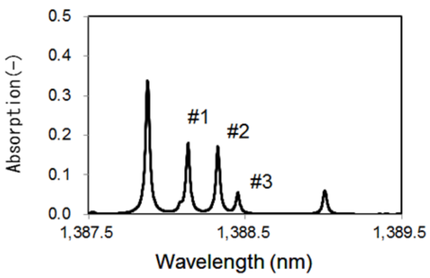


Fig. 3 Theoretical H2O absorption spectra.
(#1:1388.135nm, #2:1388.326nm, #3:1388.454nm)

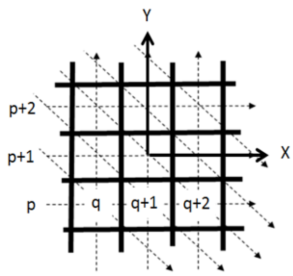


Fig. 4 laser paths and CT grid.

[DOI: 10.1299/xxx.2017xxx000x]

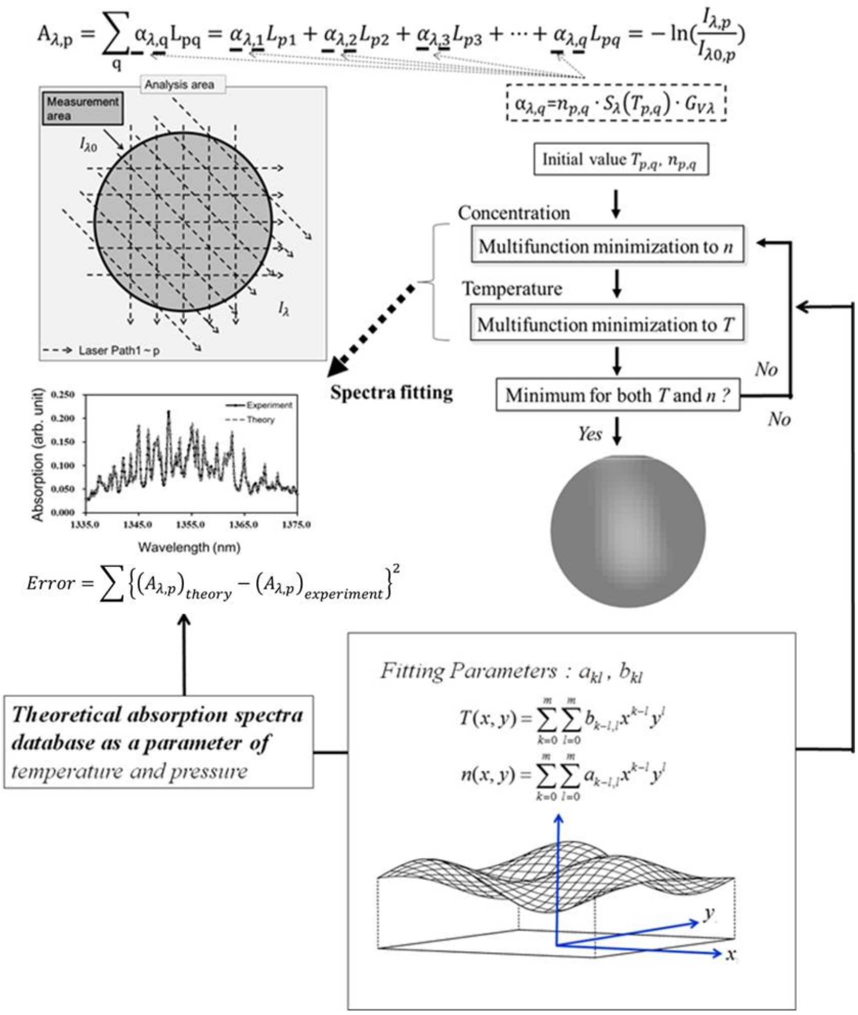


(a) Spectra fitting

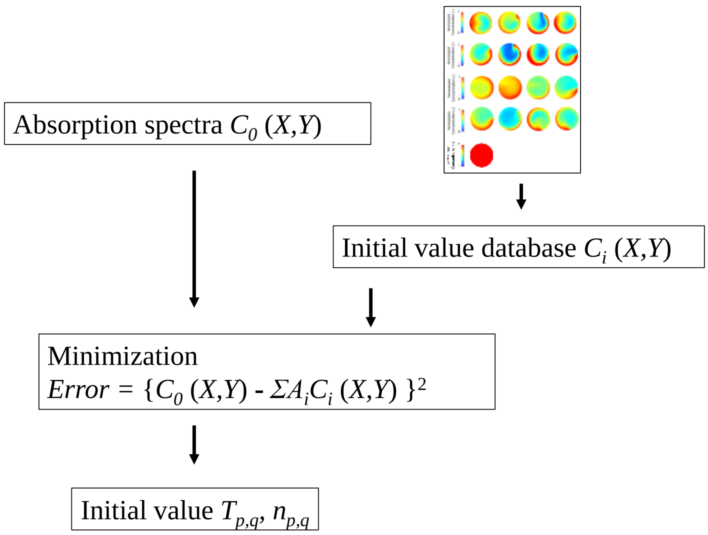


(b) Initial value setting

Fig. 5 CT algorism.

[DOI: 10.1299/xxx.2017xxx000x]

## 3. Experimental setup

Figure 6 shows a schematic of the equipment which is 2D measurement optical system. Two diode lasers at 1512nm and 1388nm which are the absorption wavelengths of $NH_3$ and $H_2O$ respectively were used to measure the absorption spectra of $NH_3$ and $H_2O$ at the same time. $H_2O$ was used to monitor the temperature distribution of the flow to consider the application to the exhaust gas conditions. In this experiment, 32-paths laser beams were passed through the $NH_3$ and air flow field. Photo diodes detected the transmitted beam intensity of each laser beam. The set of data which were stored by analyzer was used to reconstruct the concentration distribution using CT algorism.

Figure 7 shows a schematic of the experimental setup. Two 2D measurement cells were used in the bent pipe flow system and were used to measure $NH_3$ concentration distribution by CT-TDLAS as shown Fig. 7(a). This experimental system included an internal $NH_3$ jet nozzle and a bent pipe with an angle of 90°. Air was supplied through the pipe with a diameter of 60.5mm and was measured by mass flow meter to be actuated. The temperature of the flow was room temperature and it was also monitored by CT-TDLAS.

Table 1 shows experimental conditions. These conditions were also used in calculation. $NH_3$ concentration distribution through the bent pipe was measured by two 2D measurement cells using CT-TDLAS with conditions of different $NH_3$ flow rates and jet nozzle positions as shown Fig. 7(b). The experiments were carried out under ambient temperature for validation of 2D $NH_3$ measurement method using CT-TDLAS. $CH_4$ Quadruple pipes were an experiment system for the accuracy evaluation of 2D concentration measured by CT-TDLAS as shown in Fig. 8. A jet flow of 1% $CH_4$ with a buffer gas of $N_2$ was introduced into the 32 path CT-TDLAS measurement call at the flow rate of 1.7 x $10^{-5}$ $m^3/s$. The inner diameter of the jet pipe was 8 mm and the $N_2$ guard flow from an outer pipe with the inner diameter of 65 mm was formed at the flow rate of 3.3 x $10^{-4}$ $m^3/s$. The $CH_4$ concentration distribution at 3 mm above the $CH_4$ jet pipe was measured by CT-TDLAS. The $CH_4$ concentration distribution at Y=0mm was also measured by sampling the gas and measuring the $CH_4$ concentration by TDLAS.

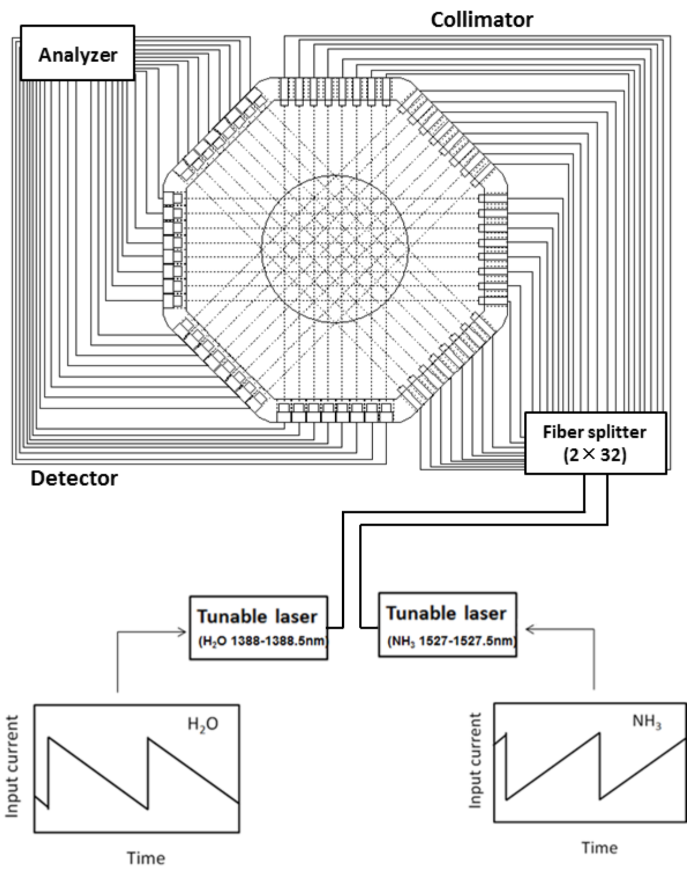


Fig. 6 Schematic of 32 paths CT-TDLAS measurement cell.

.

[DOI: 10.1299/xxx.2017xxx000x]

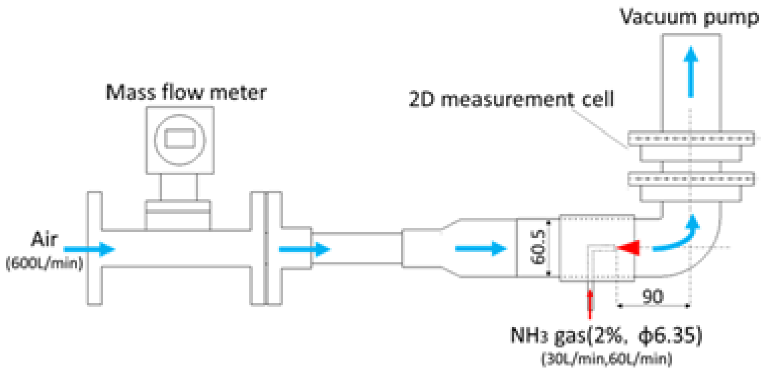


(a) Bent pipe flows system

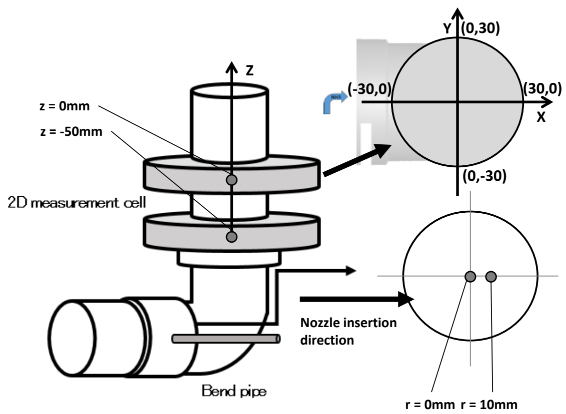


(b) $NH_3$ jet nozzle positions

Fig. 7 Schematic of the experimental setup about two cross sectional measurements.

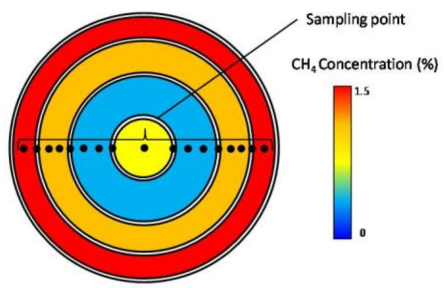


Fig. 8 Schematic of CH4 Quadruple pipes.

Table 1 Conditions of Experiment and Calculation (CFD) about two cross sectional measurement.

| | |
|---|---|
| $NH_3$ flow rate | 30L/min, 60L/min |
| Air flow rate | 600L/min |
| $NH_3$ jet nozzle position | r = 0mm, 10mm, |
| Measured field | Ordinary temperature and normal pressure |

[DOI: 10.1299/xxx.2017xxx000x]

## 4. Simulation

### 4.1 Boundary condition and basic setup

Table 2 shows CFD simulation setup and conditions. 3-D CFD simulations were conducted by the standard k-ε model using a commercial code, SCRYU/Tetra ver.12 (Software Cradle Co. Ltd). The computational grid consisted of 1.16 million tetra elements. The mesh size was 3mm and the total number of nodes was 213 thousand points. As for the boundary condition, the volume flow rate at the inlet of air was 600L/min, the volume flow rates at the inlet of $NH_3$ were 30L/min and 60L/min, the static pressure at the outlet was 0Pa, and a non-slip wall condition was applied for the pipe wall surface.

Table 2 CFD simulation setup

| Code | SCRYU/Tetra |
|---|---|
| Computational grid | 1.16 million |
| Mesh size | 3mm |
| Turbulent Model | Standard k-ε |
| Inlet boundary condition (Air) | Volume flow rate:600L/min |
| Inlet boundary condition ($NH_3$) | Volume flow rate:30L/min, 60L/min |
| Outlet boundary condition | Static pressure:0Pa |
| Wall stress | Log-law, Non-slip |

### 4.2 Governing Equations of CFD

Governing equations for this simulation include the continuous equation, the momentum equation, the diffusive species and the equation of turbulent energy and turbulent dissipation rate. They are given by the following equations, respectively.

Continuous equation:

$$\frac{\partial \rho}{\partial t}+\frac{\partial}{\partial x_i}\rho u_i=0 \tag{4}$$

Momentum equation:

$$\frac{\partial \rho u_i}{\partial t}+\frac{\partial u_j \rho u_i}{\partial x_j}=-\frac{\partial \sigma_{ij}}{\partial x_j}+\rho g_i \tag{5}$$

Diffusive species:

$$\frac{\partial \rho C}{\partial t}+\frac{\partial u_j \rho C}{\partial x_j}=\frac{\partial}{\partial x_j}\rho D_m\frac{\partial C}{\partial x_j}+\rho\dot{d} \tag{6}$$

Equation of Turbulent energy and Turbulent Dissipation Rate (k-e equations):

$$\frac{\partial \rho k}{\partial t}+\frac{\partial u_i \rho k}{\partial x_i}=\frac{\partial}{\partial x_i}\left(\frac{\mu_t}{\sigma_k}\frac{\partial k}{\partial x_i}\right)+G_S-G_{S1}-G_{S2}-G_{S3}-\rho\varepsilon \tag{7}$$

$$\frac{\partial \rho \varepsilon}{\partial t}+\frac{\partial u_i \partial \varepsilon}{\partial x_i}=\frac{\partial}{\partial x_i}\left(\frac{\mu_t}{\sigma_\varepsilon}\frac{\partial \varepsilon}{\partial x_i}\right)+C_1\frac{\varepsilon}{k}(G_s-G_{S1}-G_{S2}-G_{S3})-C_2\frac{\rho\varepsilon^2}{k} \tag{8}$$

$$G_S=\mu_t\left(\frac{\partial u_i}{\partial x_j}+\frac{\partial u_j}{\partial x_i}\right)\frac{\partial u_i}{\partial x_j},\qquad G_{S1}=\frac{2}{3}\rho k\frac{\partial u_i}{\partial x_i},\qquad G_{S2}=\frac{2}{3}\mu_t(\frac{\partial u_i}{\partial x_i})^2,\qquad G_{S3}=\frac{\mu_t}{\sigma_t\rho^2}\frac{\partial \rho}{\partial x_i}\frac{\partial P}{\partial x_i} \tag{9}$$

| $\sigma_k$ | $\sigma_\varepsilon$ | $C_1$ | $C_2$ | $C_3$ | $C_\mu$ | $\sigma_t$ |
|---|---|---|---|---|---|---|
| 1 | 1.3 | 1.44 | 1.92 | 0.0 | 0.09 | 0.9 |

[DOI: 10.1299/xxx.2017xxx000x]

## 5. Results and discussions

### 5.1 Evaluation of CT reconstruction accuracy

In order to evaluate the accuracy of CT reconstruction, three factors have been tested. The first is the special resolution of CT reconstruction. The concentration profiles having different FWHM values from the original profiles were generated. Then the CT reconstructed profiles were compared with the original profiles. The second is SSD (sum of squared difference). The SSD value has been defined by Eq. (10). If the SSD value is close to “0”, the two profiles have almost same values. The third is ZNCC (zero-mean normalized cross-correlation) shown in Eq. (11) and Eq. (12). If this value close to “1”, he two profiles have almost same patterns and the correlation between the two profiles is very high.

$$SSD = \sqrt{\frac{\sum_{i=0}^{N-1}\sum_{j=0}^{M-1}\left\{(n_{i,j})_{virtual} - (n_{i,j})_{CT-TDLAS}\right\}^2}{NM}} \Big/ n_R \tag{10}$$

$$ZNCC = \frac{\sum_{i=0}^{N-1}\sum_{j=0}^{M-1}\left\{(n_{i,j} - \bar{n})_{virtual} \times (n_{i,j} - \bar{n})_{CT-TDLAS}\right\}}{\sqrt{\sum_{i=0}^{N-1}\sum_{j=0}^{M-1}(T_{i,j} - \bar{n})_{virtual}{}^2 \times \sum_{i=0}^{N-1}\sum_{j=0}^{M-1}(n_{i,j} - \bar{n})_{CT-TDLAS}{}^2}}, \tag{11}$$

$$\bar{n} = \frac{\sum_{i=0}^{N-1}\sum_{j=0}^{M-1} n_{i,j}}{NM} \tag{12}$$

Here, $n_{i,j}$ is the temperature at each point in calculation area, $n_R$ is the representing concentration, $N$ is the total number of meshes along the X-axis in the calculation area, and $M$ is the total number of meshes along the Y-axis in the calculation.

Figure 9 show the profile of original(Gaussian distribution) and CT reconstruction. These were different FWHM values (Original:12mm, CT reconstruction:13.2mm) . However, These profiles are very similar. Therefore, CT reconstruction had the resolution of FWHM 12mm.

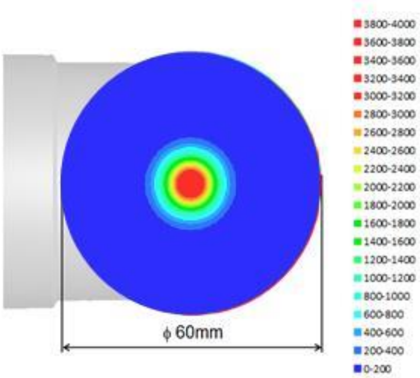


(a) Original profiles
(Gaussian distribution FWHM:12mm)

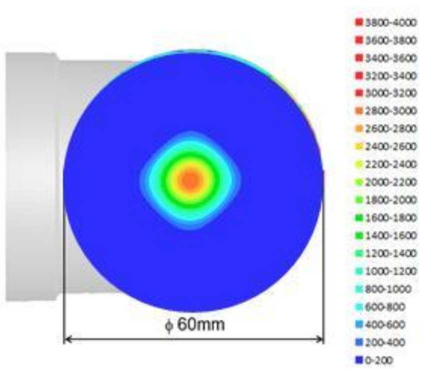


(b) CT reconstruction profiles
(FWHM:13.2mm)

Fig. 9 FWHM evaluation of CT reconstruction accuracy.

Table 3 shows conditions of CFD which was simulated as two cross-sectional measurements and Table 3 shows the SSD and ZNCC evaluation between CFD and theoretical results of $NH_3$ concentration distribution about each

[DOI: 10.1299/xxx.2017xxx000x]

evaluation points. Theoretical results were reconstructed from CFD results for evaluating accuracy of CT. All of SSD values were less than 0.1. And All of ZNCC values except one condition (30L/min, r=10mm, Z=-50mm) were larger than 0.9. In addition, Fig. 10-13 represent that theoretical results agreed to CFD results.

Table 3 SSD and ZNCC evaluations between CFD and theoretical (CT reconstruction) results.

| Evaluate all measurement points(39x39=1521) | | | | |
|---|---|---|---|---|
| NH3 flow | Nozzle position | Cell position | SSD | ZNCC |
| 30L/min | r = 0mm | Z=0mm | 0.0295 | 0.947 |
| 30L/min | r = 10mm | Z=0mm | 0.0307 | 0.981 |
| 60L/min | r = 0mm | Z=0mm | 0.0092 | 0.980 |
| 60L/min | r = 10mm | Z=0mm | 0.0171 | 0.989 |
| 30L/min | r = 0mm | Z=-50mm | 0.0825 | 0.890 |
| 30L/min | r = 10mm | Z=-50mm | 0.0758 | 0.940 |
| 60L/min | r = 0mm | Z=-50mm | 0.0265 | 0.912 |
| 60L/min | r = 10mm | Z=-50mm | 0.0338 | 0.971 |

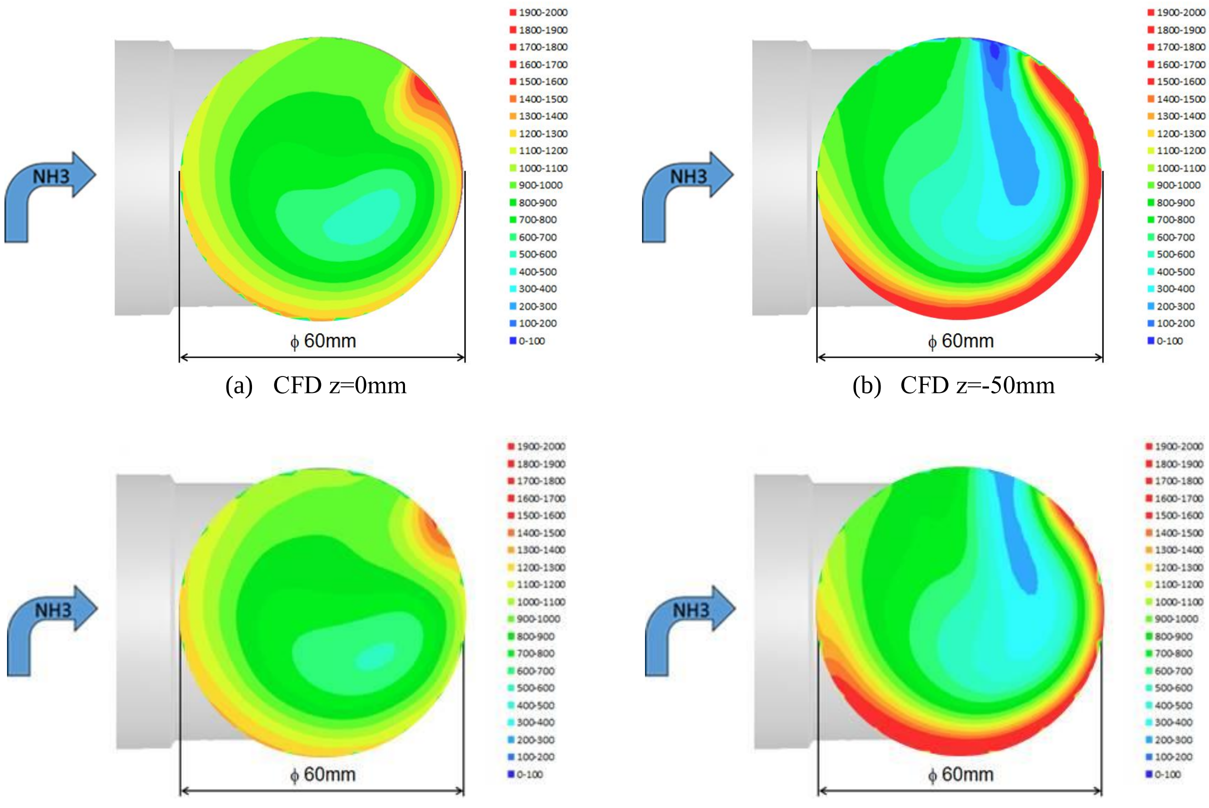


(a) CFD z=0mm (b) CFD z=-50mm

(c) Theoretical z=0mm (d) Theoretical z=-50mm

Fig. 10 2D concentration distribution of $NH_3$ by CFD and theoretical(r=0mm, 30L/min).

[DOI: 10.1299/xxx.2017xxx000x] 

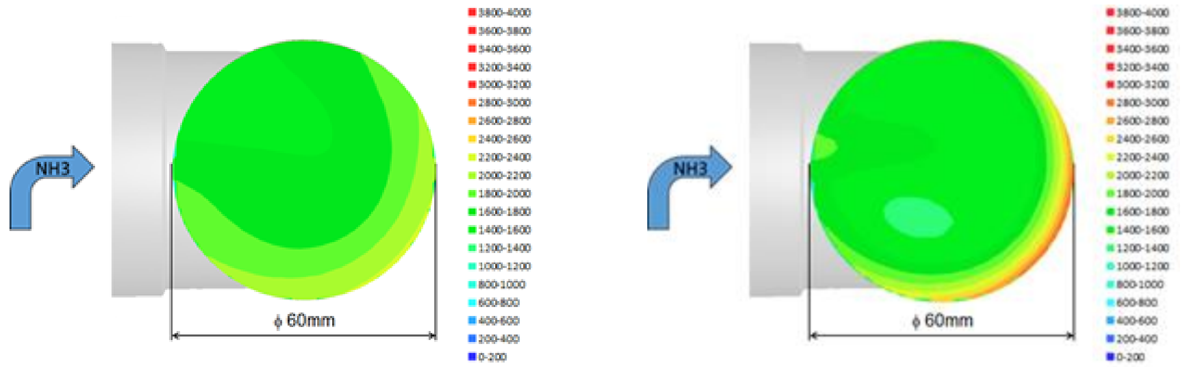


(a) CFD z=0mm (b) CFD z=-50mm

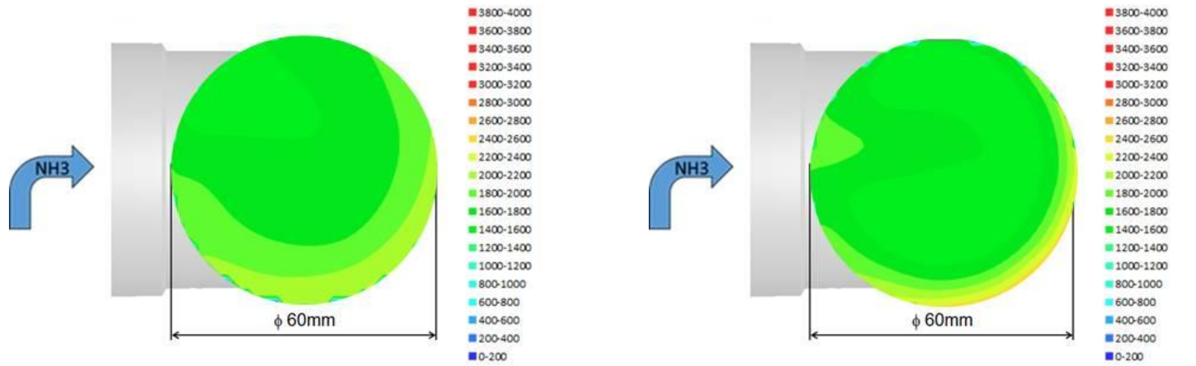


(c) Theoretical z=0mm (d) Theoretical z=-50mm

Fig. 11 2D concentration distribution of $NH_3$ by CFD and theoretical (r=0mm, 60L/min).

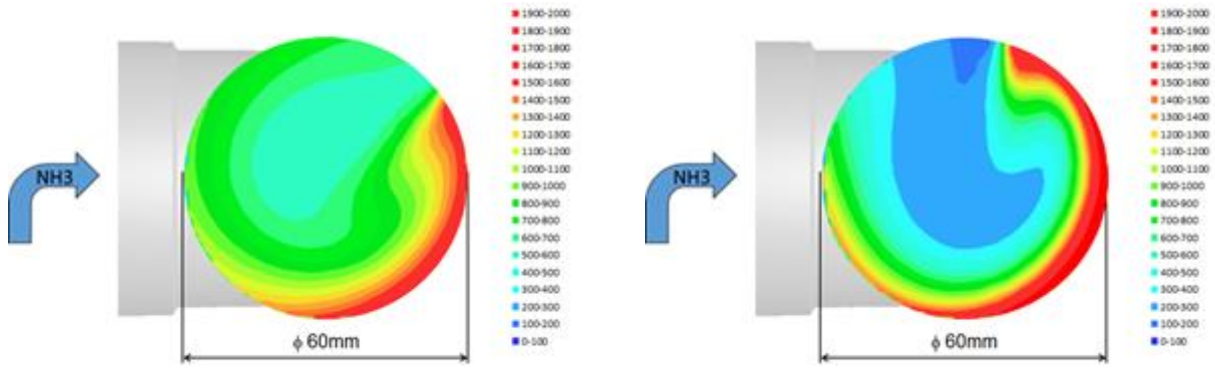


(a) CFD z=0mm (b) CFD z=-50mm

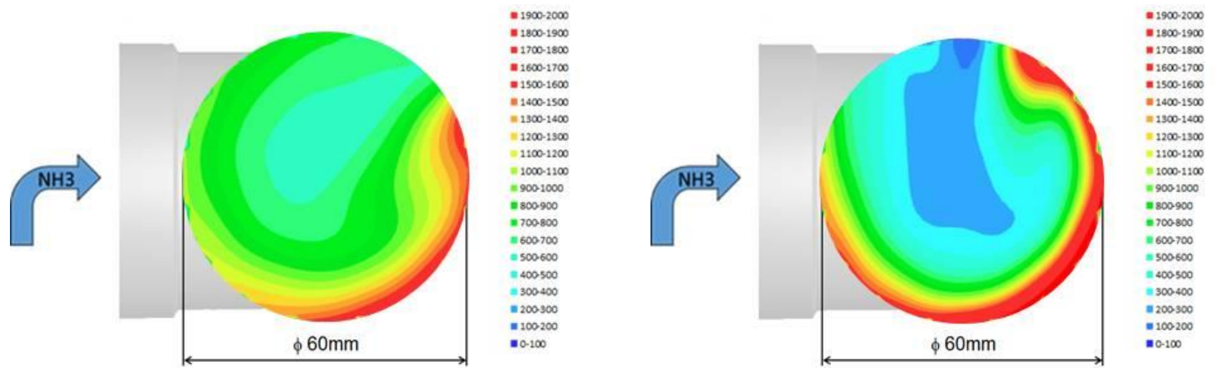


(c) Theoretical z=0mm (d) Theoretical z=-50mm

Fig. 12 2D concentration distribution of $NH_3$ by CFD and theoretical(r=10mm, 30L/min).

[DOI: 10.1299/xxx.2017xxx000x]

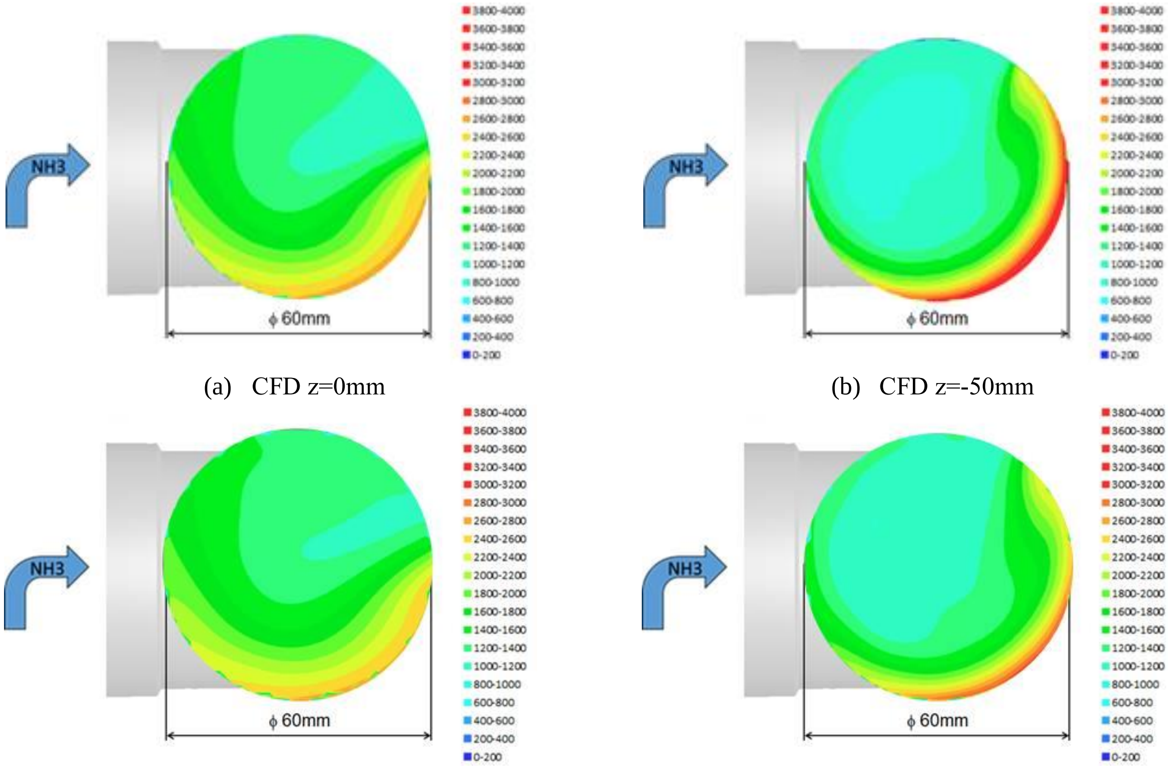


(a) CFD z=0mm

(b) CFD z=-50mm

(c) Theoretical z=0mm

(d) Theoretical z=-50mm

Fig. 13 2D concentration distribution of $NH_3$ by CFD and theoretical (r=10mm, 60L/min).

### 5.2 Measurement of $CH_4$ quadruple pipes

Figure 14-15 show results of $CH_4$ concentration distribution by quadruple pipes. Figure 14(a) was constructed by sampling results and Fig. 14(b)-(d) were reconstructed concentration distributions of $CH_4$ by CT. Figure 14(d) agrees to Fig. 14(a) more than other cases. In addition, Fig. 15 represents 14th order reconstruction matches the sampling results. Therefore, these results show that 14th order polynomial is needed to reconstruct the test sampling results.

### 5.3 Two Cross-sectional measurement of $NH_3$

Figure 16-19 represents two cross-sectional 2D concentration distributions of $NH_3$ measured by CT-TDLAS and table 1 shows conditions of measurements same as CFD. There are high $NH_3$ concentration zones near the pipe wall in all conditions and sections, and the locations of high concentration zones differ depending on conditions and sections. However, the locations of high $NH_3$ concentrations by CT-TDLAS and CFD are very close by comparing with each condition and section. In addition, 2D concentrations of distribution of $NH_3$ by CT-TDLAS have similar characteristics about flow patterns to those by CFD at each condition and section in Fig. 10-13 and Fig. 16-19.

Figure 20-23 show two cross sectional 1D concentration (y=0mm) of $NH_3$ measured by CT-TDLAS and calculated results. There are some differences between CT-TDLAS and CFD results. However, these $NH_3$ concentrations show similar trends which there are high concentration near the pipe wall area (x=-30, 30).

On the other hand, distribution trends of measured and calculated have two differences depending on sections. Firstly, upper section (z=0mm) results of $NH_3$ concentration uniformity are higher than lower section (z=-50mm) results of $NH_3$ concentration uniformity in each condition in Fig. 16-19. Secondly upper section results of high $NH_3$ concentration zone rotate by some angle from lower sections results of high $NH_3$ concentration zone in Fig. 18-19. These phenomena are caused by effects of swirl flow. Both of measured and calculated results show these characteristics in this study.

CT-TDLAS is the measurement method combining two theories. These methods include some errors which affect measurement accuracy. TDLAS can measure $NH_3$ concentration with high accuracy because of very strong correlation

[DOI: 10.1299/xxx.2017xxx000x]

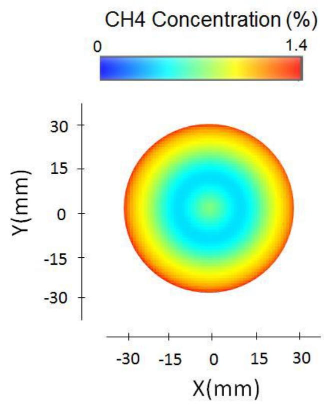


(a) Test Sampling result

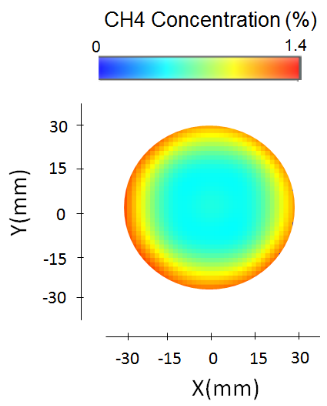


(b) CT-TDLAS(8th)

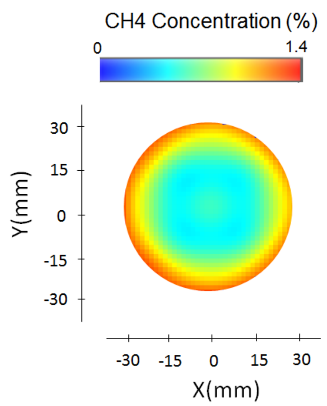


(c) CT-TDLAS(10th)

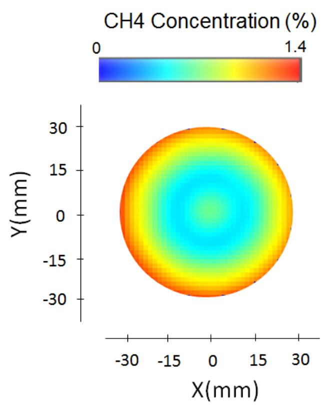


(d) CT-TDLAS(14th)

Fig. 14 2D concentration distribution of CH4 by quadruple pipes.

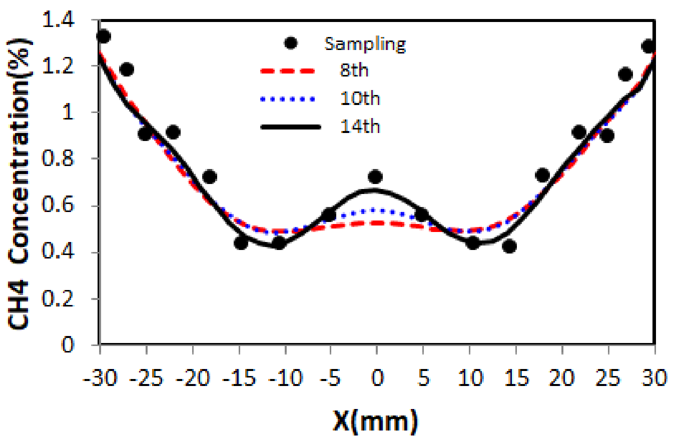


Fig. 15 Sampling and CT reconstruction results.

($R^2$ = 0.9978) between $NH_3$ concentration and absorbance as shown in Fig. 2 (b). In addition, Fig. 10-13 and Table 4 show that CT has enough accuracy to reconstruct the concentration distributions of $NH_3$. The vibrations of pipe didn't affect the measurement accuracy. The measurement cells were fixed to the pipe and the positional relationship between the pipe and the cells were always unchanged during the vibrations of the total systems. This method has already applied to the temperature measurement in engine cylinder and it was demonstrated that the temperature distribution was successfully measured with the vibrations of an engine which was bigger compared those in the pipe (Deguchi, 2017).

[DOI: 10.1299/xxx.2017xxx000x]

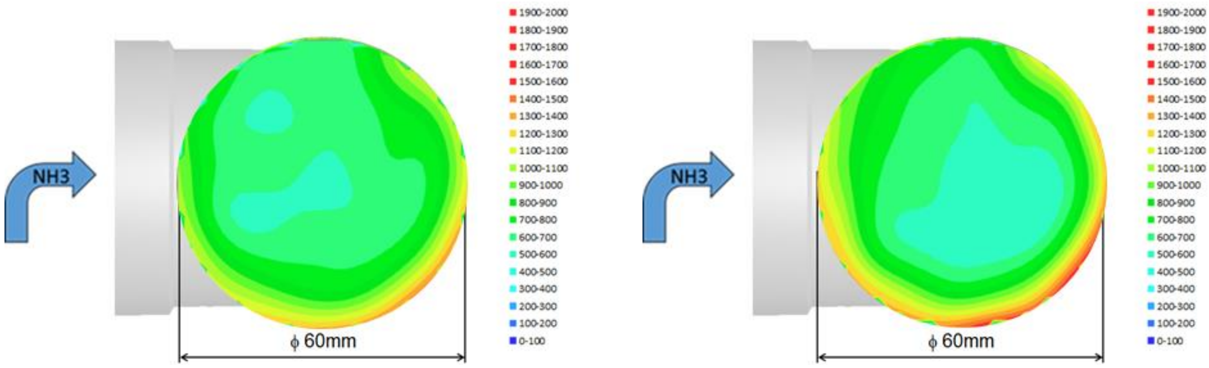


(a) CT-TDLAS z=0mm (b) CT-TDLAS z=-50mm

Fig. 16 2D concentration distribution of $NH_3$ by CT-TDLAS (r=0mm, 30L/min).

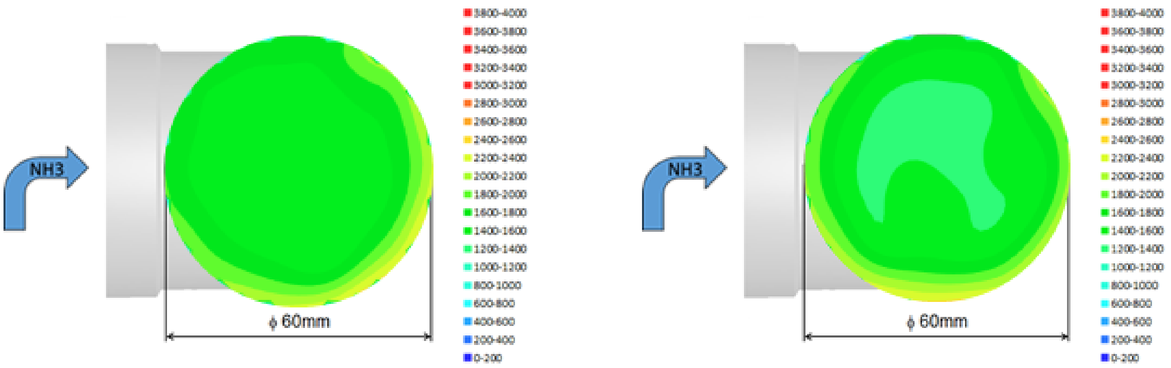


(a) CT-TDLAS z=0mm (b) CT-TDLAS z=-50mm

Fig. 17 2D concentration distribution of $NH_3$ by CT-TDLAS (r=0mm, 60L/min).

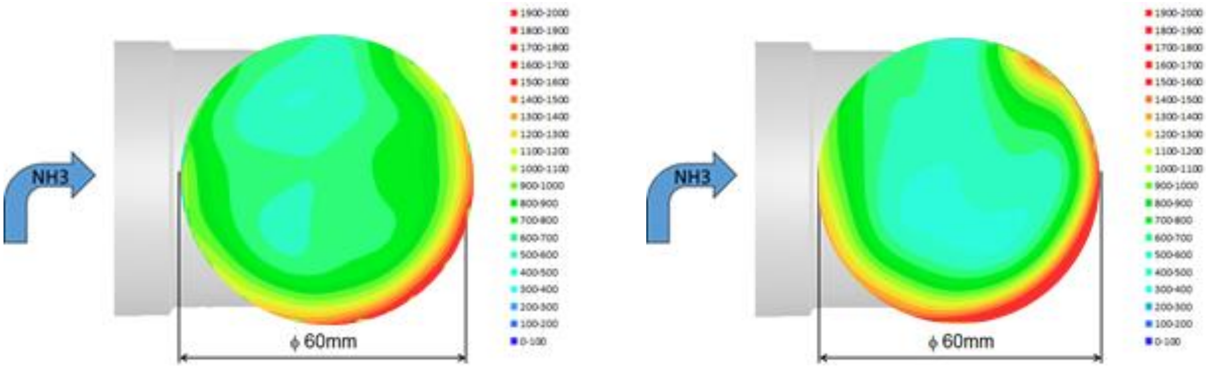


(a) CT-TDLAS z=0mm (b) CT-TDLAS z=-50mm

Fig. 18 2D concentration distribution of $NH_3$ by CT-TDLAS(r=0mm, 30L/min).

[DOI: 10.1299/xxx.2017xxx000x] 

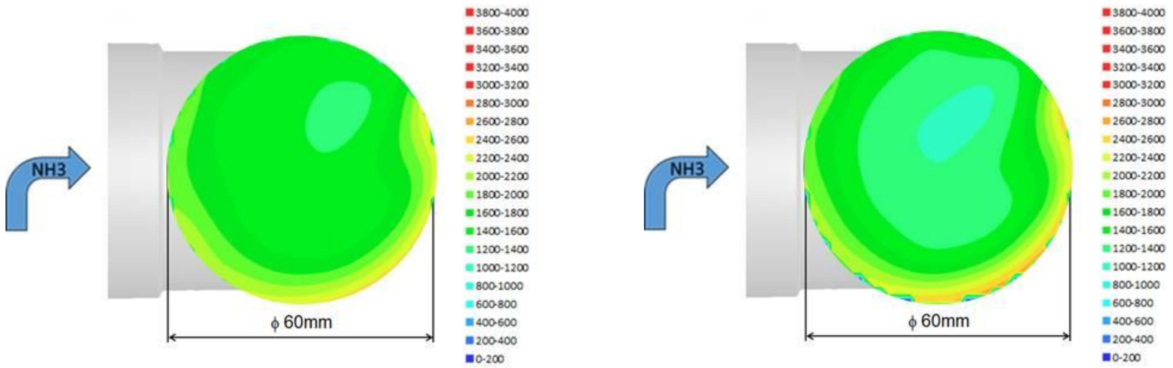


(a) CT-TDLAS z=0mm (b) CT-TDLAS z=-50mm

Fig. 19 2D concentration distribution of $NH_3$ by CT-TDLAS (r=10mm, 60L/min).

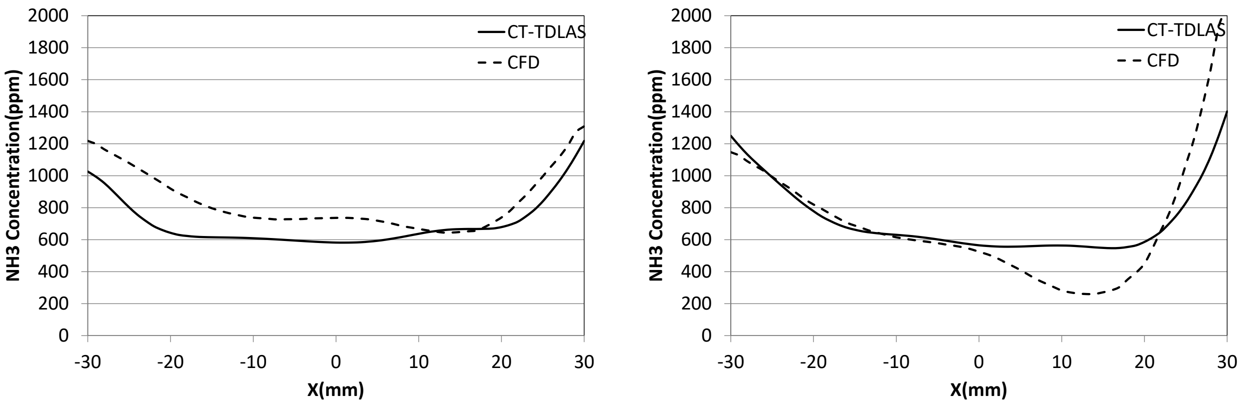


(a) z=0mm (b) z=-50mm

Fig. 20 1D concentration distribution of $NH_3$ by CT-TDLAS and CFD (y=0mm, r=0mm, 30L/min).

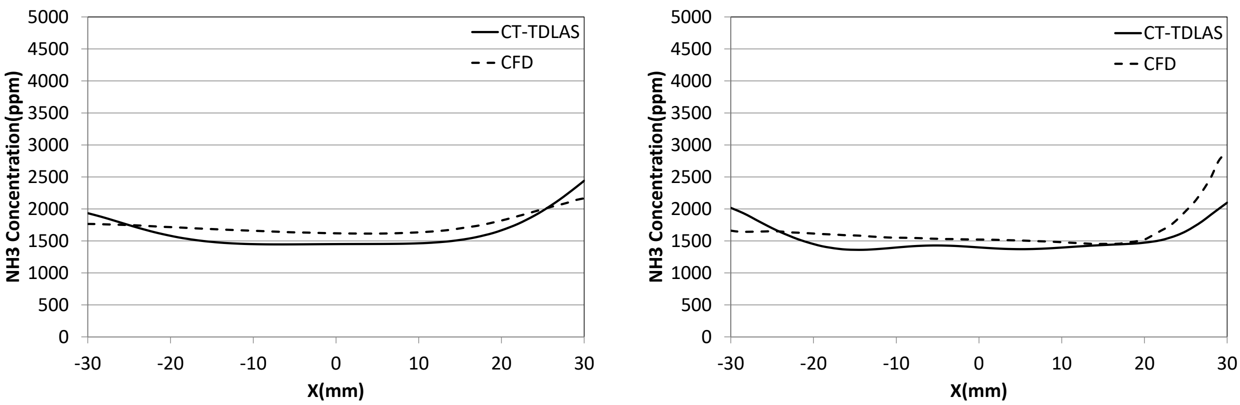


(a) z=0mm (b) z=-50mm

Fig. 21 1D concentration distribution of $NH_3$ by CT-TDLAS and CFD (y=0mm, r=0mm, 60L/min).

[DOI: 10.1299/xxx.2017xxx000x]

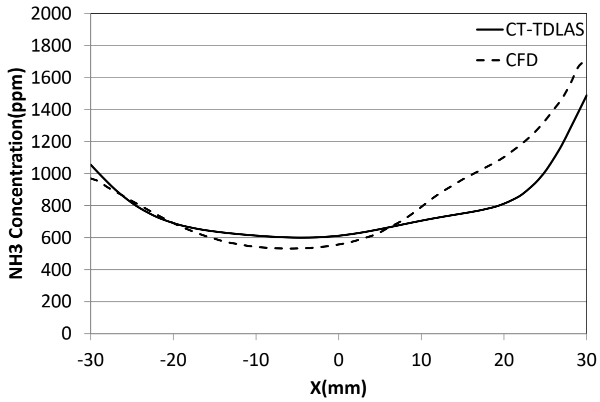


(a) z=0mm

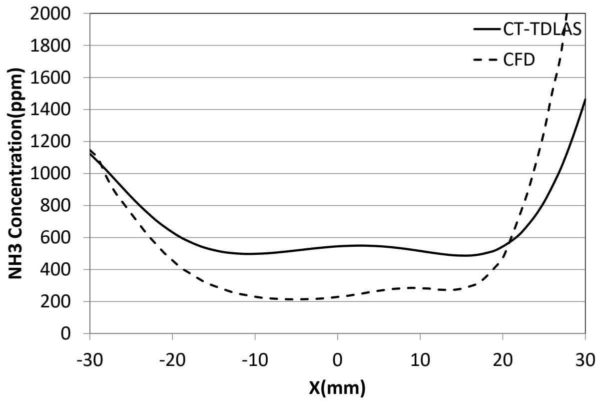


(b) z=-50mm

Fig. 22 1D concentration distribution of $NH_3$ by CT-TDLAS and CFD (y=0mm, r=10mm, 30L/min).

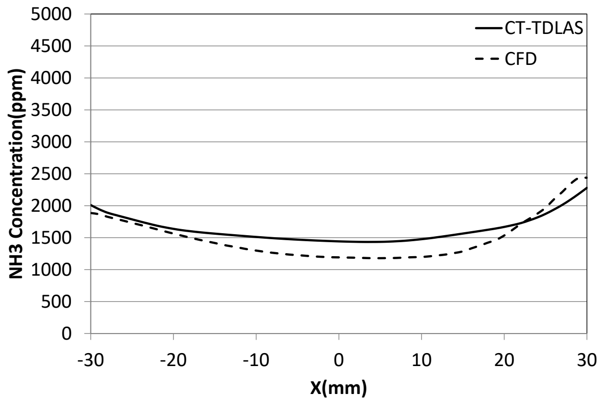


(a) z=0mm

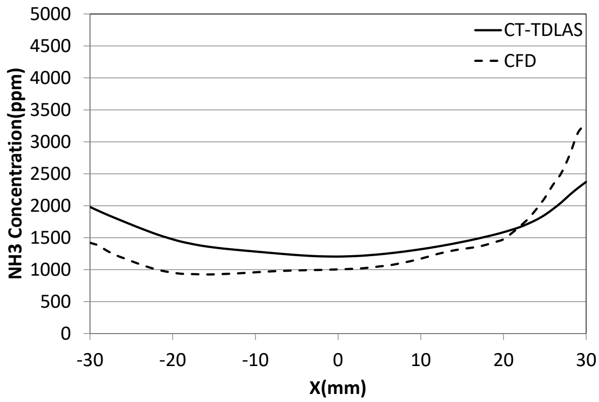


(b) z=-50mm

Fig. 23 1D concentration distribution of $NH_3$ by CT-TDLAS and CFD (y=0mm, r=10mm, 60L/min).

Table 4 Comparison between CFD and CT-TDLAS Measurement Results.

| Evaluate all measurement points(39x39=1521) | | | | | |
|---|---|---|---|---|---|
| NH3 flow | Nozzle position | Cell position | CFD – CT Reconstruction standard deviation (ppm) (A) | Max concentration (ppm) (B) | (A) / (B) (%) |
| 30L/min | r = 0mm | Z=0mm | 37.3 | 1614 | 2.3 |
| 30L/min | r = 10mm | Z=0mm | 37.5 | 1823 | 2.1 |
| 60L/min | r = 0mm | Z=0mm | 16.6 | 2242 | 0.7 |
| 60L/min | r = 10mm | Z=0mm | 39.3 | 2709 | 1.5 |
| 30L/min | r = 0mm | Z=-50mm | 105.4 | 2115 | 5.0 |
| 30L/min | r = 10mm | Z=-50mm | 120.2 | 2870 | 4.2 |
| 60L/min | r = 0mm | Z=-50mm | 66.3 | 2996 | 2.2 |
| 60L/min | r = 10mm | Z=-50mm | 86.2 | 3576 | 2.4 |

## 6. Conclusions

The following results were obtained from the two cross-sectional 2D concentration distributions of $NH_3$ results by CT-tunable diode laser absorption spectroscopy.

The CFD and theoretical results of two cross-sectional 2D concentration of $NH_3$ and $CH_4$ quadruple pipes results show that CT-TDLAS have the enough accuracy for measuring the concentration distribution of $NH_3$ in pipes. And measuring simultaneous two cross-sectional 2D concentration distribution of $NH_3$ enables to observe not only concentration distribution but also detail flow pattern like swirl flow in bent pipe.

The results of this study show the possibility of observing flow patterns or characteristics of $NH_3$. Therefore, this study helps to improve the accuracy of CFD by applying a real diesel engine including urea SCR system. And it helps to improve the efficiency of urea SCR by using CFD for designing.

## References

An, X., Kraetschmer, T., Takami, K., Sanders, S. T., Ma, L., Cai, W., Li, X., Roy, S. and Gord, J. R., Validation of temperature imaging by $H_2O$ absorption spectroscopy using hyperspectral tomography in controlled experiments, *Applied Optics, Vol. 50, No.40* (2011), A29-A37.

An, X., Brittelle, M. S., Lauzier, P. T., Gord, J. R., Roy, S., Chen, G. and Sanders, S. T., Demonstration of temperature imaging by $H_2O$ absorption spectroscopy using compressed sensing tomography, *Applied Optics, Vol.54, No.31* (2015), pp. 9190-9199.

Cai, W. and Kaminski, C.F., A tomographic technique for the simultaneous imaging of temperature, chemical species, and pressure in reactive flows using absorption spectroscopy with frequency-agile lasers, *Applied Physics Letters, Vol.104, No.3,* (2015), 034101.

Deguchi, Y., Industrial applications of Laser Diagnostics (2011) CRS Press; Taylor & Francis: New York, USA.

Deguchi Y., Yasui D. and Adachi A.: Development of 2D temperature and concentration measurement method using tunable diode laser absorption spectroscopy, *Journal of Mechanics Engineering and Automation, Vol.2, No.9*(2012), pp.543-549.

Deguchi, Y., Kamimoto, T. and Kiyota, Y., Time resolved 2D Concentration and temperature measurement using CT tunable laser absorption spectroscopy, *Flow Measurement and Instrumentation, Vol.46,Part B (*2015), pp. 312-318.

Deguchi, Y., Kakagi, T., Kamimoto, T., Okamoto T and Watanabe N., Time-series Two-dimensional Temperature Measurement Inside the Engine Cylinder Using Computed Tomography-Tunable Diode Laser Absorption Spectroscopy, *Transactions of the Society of Automotive Engineers of Japan, Vol.48,No.1, (*2017), pp. 35-40.

Kamimoto T., Deguchi Y. and Kiyota Y., High temperature field application of two dimensional temperature measurement technology using CT tunable laser absorption spectroscopy, *Flow Measurement and Instrumentation, Volume 46, Part A* (2015) , pp. 51–57.

Kamimoto, T., Deguchi, Y., Choi, D. and Shim, J., Validation of real-time 2D temperature measurement method using CT tunable diode laser absorption spectroscopy, *Heat Transfer Research, Vol.47, No.2* (2016), pp. 193-202.

Kasyutich, V.L., and Martin, P.A., Towards a two-dimensional concentration and temperature laser absorption tomography sensor system, *Applied Physics B: Lasers and Optics, Vol. 102, No.1* (2011), pp. 149-162.

Jatana, G.S., Magee, M. , Fain, D. , Naik, S.V., Shaver, G.M. and Lucht, R.P., Simultaneous high-speed gas property measurements at the exhaust gas recirculation cooler exit and at the turbocharger inlet of a multicylinder diesel engine using diode-laser-absorption spectroscopy, *Applied Optics, Vol.54, No.5 (*2015), pp. 1220-1231.

Ma, L. and Cai, W., Numerical investigation of hyperspectral tomography for simultaneous temperature and concentration imaging, *Applied Optics, Vol. 47, No.21* (2008), pp. 3751-3759.

Ma, L., Li, X., Sanders, S.T., Caswell, A.W., Roy, S., Plemmons, D.H. and Gord, J.R., 50-kHz-rate 2D imaging of temperature and $H_2O$ concentration at the exhaust plane of a J85 engine using hyperspectral tomography, *Optics Express, Vol. 21, No.1* (2013), pp. 1152-1162.

McCann, H., Wright, P. and Daun, K., *Industrial Tomography: Systems and Applications* (2015) Inc. Elsevier: Cambridge, UK, pp. 135-174.

Rieker, G.B., Li, H., Liu, X., Liu, J.T.C., Jeffries, J.B., Hanson, R.K., Allen, M.G., Wehe, S.D., Mulhall, P.A., Kindle, H.S, Kakuho., A, Sholes, K.R., Matsuura, T. and Takatani S., Rapid measurements of temperature and $H_2O$ concentration in IC engines with a spark plug-mounted diode laser sensor, *Proceedings of the Combustion Institute, Vol. 31, No.2* (2007), pp. 3041–3049.

Rothman, L.S., Gordon, I.E., Barbe, A., ChrisBenner, D., Bernath, P.F., Birk, M., Boudon, V., Brown, L.R., Campargue, A., Champion, J.P., Chance, K., Coudert, L., Dana, V., Devi, V.M., Fally, S., Flaud, J.M., Gamache, R.R., Goldman, A., Jacquemart, D., Kleiner, I., Lacome, N., Lafferty, W.J., Mandin, J.-Y., Massie, S.T., Mikhailenko, S.N., Miller,

[DOI: 10.1299/xxx.2017xxx000x] 

C.E., Moazzen-Ahmadi, N., Naumenko, O.-V., Nikitin, A.V., Orphal, J., Perevalov, V.I., Perrin, A., Predoi-Cross, A., Rinsland, C.P., Rotger, M., Simeckova, M., Smith, M.A.H., Sung, K., Tashkun, S.A., Tennyson, J., Toth, R.A., Vandaele, A.C., and VanderAuwera, J., The HITRAN2008 molecular spectroscopic database, Journal of Quantitative Spectroscopy & Radiative Transfer, *Vol.* 110 (2009), pp. 533-572.

Seidel, A., Wagner, S., Dreizler, A. and Ebert, V., Robust, spatially scanning, open-path TDLAS hygrometer using retro-reflective foils for fast tomographic 2-D water vapor concentration field measurements, *Atmospheric Measurement Techniques, Vol. 8, No.5* (2015), pp. 2061-2068.

Stritzke, F., Diemel, O., and Wagner, S., TDLAS-based NH3 mole fraction measurement for exhaust diagnostics during selective catalytic reduction using a fiber-coupled 2.2-µm DFB diode laser, *Applied Physics B: Lasers and Optics, Vol. 119, No.1* (2015), pp. 143-152.

Wang, F., Cen, K., F, Li, N., Jeffries, J. B., Huang, Q. X, Yan, J. H. and Chi, Y., Two-dimensional tomography for gas concentration and temperature distributions based on tunable diode laser absorption spectroscopy, *Measurement Science and Technology, Vol.21, No.4, (2010),* 045301.

Wright, P., Terzijaa, N., Davidsona, J. L., Garcia-Castillo, S., Garcia-Stewart, C., Pegrumb, S., Colbourneb, S., Turnerb P., Crossleyc, S. D., Litt, T., Murrayc, S., Ozanyana, K. B. and McCanna, H., High-speed chemical species tomography in a multi-cylinder automotive engine, *Chemical Engineering Journal, Vol.158, No.1* (*2010),* pp 2–10.

Yamakage, M., Muta, K., Deguchi, Y., Fukada, S., Iwase T. and Yoshida T, Development of direct and fast response exhaust gas measurement *Flow Measurement and Instrumentation SAE Paper (2008), 20081298.*

[DOI: 10.1299/xxx.2017xxx000x] 